PCCP

PAPER

Cite this: *Phys. Chem. Chem. Phys.*, 2017, **19**, 5366

Structure and dysprosium dopant engineering of gadolinium oxide nanoparticles for enhanced dual-modal magnetic resonance and fluorescence imaging†

Jinchang Yin, Chaorui Li, Deqi Chen, Jiajun Yang, Huan Liu, Wenyong Hu and Yuanzhi Shao*

Received 30th September 2016,
Accepted 23rd January 2017

DOI: 10.1039/c6cp06712c

rsc.li/pccp

We report a class of multi-functional core–shell nanoarchitectures, consisting of silica nanospheres as the core and Gd_2O_3:Dy^{3+} nanocrystals as the ultra-thin shell, that enable unique multi-color living cell imaging and remarkable *in vivo* magnetic resonance imaging. These types of targeted cell imaging nanoarchitectures can be used as a variety of fluorescence nanoprobes due to the multi-color emissions of the Gd_2O_3:Dy^{3+} nanophosphor. We also proposed a strategy of modulating core–shell structure design to achieve an enhanced magnetic resonance contrast ability of Gd_2O_3 nanoagents, and the classical Solomon–Bloembergen–Morgan theory was applied to explicate the mechanism underlying the enhancement. The as-synthesized ligand-free nanomaterial possesses a suitable particle size for cellular uptake as well as avoiding penetrating the blood–brain barrier with good water-solubility, stability, dispersibility and uniformity. The extremely low cytotoxicity and favorable biocompatibility obtained from *in vitro* and *in vivo* bioassays of the as-designed nanoparticles indicate their excellent potential as a candidate for functioning as a targeted nanoprobe.

Introduction

Magnetic resonance imaging (MRI) is a routine non-invasive clinical diagnosis technique based on the magnetic properties of hydrogen nuclei existing in human body tissues.[1–4] Contrast agents (CAs) are commonly injected into the body to affect the magnetization and relaxation of protons, causing a high imaging contrast in target tissues (*i.e.* tumors, liver, kidneys, spleen, *etc.*), even at molecular and cellular levels.[5,6] Conventional paramagnetic gadolinium chelated complexes, in spite of their non-toxicity and water-solubility, could not meet the needs of growing demands in the biomedical field because of their low relaxivity and non-targeted functionality.[7–9] Gadolinium oxide (Gd_2O_3) nanoparticles (NPs) are emerging as potential targeted MRI-CAs with a rather high longitudinal relaxivity (r_1), and they can rapidly shorten the spin–lattice relaxation time (T_1) of the surrounding water protons and be transported to the reticuloendothelial system more than the vasculature, generating a specific biodistribution before being completely excreted through the renal system.[10,11] Recently, ultra-small Gd_2O_3 nanoparticle colloids have been developed successfully, and they display a rather high longitudinal relaxivity due to their ultra-high surface to volume (S/V) ratio.[12–15]

Unfortunately, ultra-small Gd_2O_3 particles can pass through the blood–brain barrier (BBB) and some of them readily deposit in the brain like gadolinium chelates.[16–19] Moreover, they have a short half-life in the blood and thus repeated injections and large dosages have to be used in clinical operations, which may cause an undesirable false-positive contrast enhancement. Fortunately, 100 nm NPs with a long blood half-life have been introduced to overcome these deficiencies. Usually, NPs around 100 nm cannot penetrate the BBB but can still flow in the body instead.[20] However, 100 nm Gd_2O_3 NPs possess a lower relaxivity because of a lower S/V ratio in comparison to ultra-small Gd_2O_3 NPs. Here we report a design strategy (Fig. 1) to construct a novel T_1-weighted contrast agent that retains a high longitudinal relaxivity r_1 in light of the Solomon–Bloembergen–Morgan (SBM) theory,[21–26] a classical theory underlying the relaxation changes of water protons in the presence of CAs. We encapsulated SiO_2 nanospheres with an ultra-thin nanoshell of ligand-free Gd_2O_3. The thinner the nanoshells are, the higher the relaxivity of the nanocomposite is. This is an excellent approach to increase the portion of Gd^{3+} ions located on the surfaces of the NPs.

School of Physics, State Key Laboratory of Optoelectronic Materials and Technologies, Sun Yat-sen University, Guangzhou 510275, P. R. China. E-mail: stssyz@mail.sysu.edu.cn

† Electronic supplementary information (ESI) available: XRD, SEM, EDX, FTIR, TG-DTA, excitation and emission spectra, confocal laser microscopy, images of samples dissolved in aqueous solutions, and *in vitro* and *in vivo* T_1-weighted MR phantom images. See DOI: 10.1039/c6cp06712c

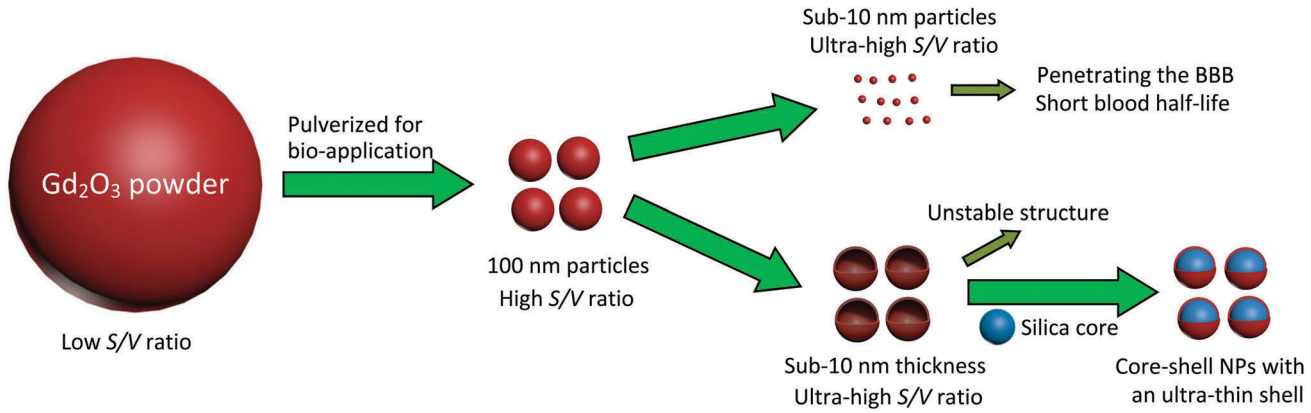

Fig. 1 Schematic illustration of the proposed design strategy to construct the ligand-free core–shell gadolinia-based NPs with an ultra-thin shell for maintaining an ultra-high longitudinal relaxivity. The 100 nm core–shell NPs possess a long blood half-life and cannot penetrate the BBB due to their large grain size; moreover they possess an ultra-high r_1 owing to the ultra-high *S/V* ratio induced by the ultra-thin gadolinia nanoshell.

Apparently, more Gd^{3+} ions could stay on the thinner nanoshells, facilitating the spin–lattice relaxation of water protons caused by the involvement of Gd^{3+} ions.[27–30]

Fluorescent magnetic NPs that serve as multi-modal CAs have drawn much attention in the past two decades.[31–38] The greatest advantage of MRI in clinical bioimaging is its instinctive high spatial resolution (50 μm), which is much higher than that of fluorescence imaging (FI) whose resolution is about 1–2 mm. However, MRI sensitivity is merely up to 10^{-9}–10^{-6} moles for biolabel detection, relatively lower than that of FI (nearly 10^{-12} moles).[39,40] Therefore, dual-modal CAs combining MRI and FI can readily achieve a high spatial resolution and large sensitivity simultaneously, which is intensively demanded in biomedical imaging.

Generally, gadolinium oxide is an excellent host matrix for down- and up-conversion photoluminescence of the activated lanthanide ions (*i.e.* Eu^{3+}, Tb^{3+}, Dy^{3+} and Yb^{3+}/Er^{3+}, Yb^{3+}/Ho^{3+}, Yb^{3+}/Tm^{3+}, *etc.*)[41–45] owing to its low phonon energy and desirable chemical stability. Rare-earth ion doped photoluminescent nanomaterials used in bioimaging and biolabeling have aroused a great deal of interest from researchers, and they have been extensively investigated during the past few decades due to their lower cytotoxicity and superior chemical stability in contrast to semiconducting quantum dots (QDs)[46–49] and their excellent photostability, narrow absorption and emission spectra, long lifetimes, large Stokes shifts and minimized photobleaching, as compared to conventional luminescent labeling organic dyes.[50–53] Among those lanthanide ions, Dy^{3+} is unique for its photoluminescence and magnetic properties. Gd_2O_3:Dy^{3+} NPs for multi-color living cell imaging have been proposed and investigated in recent research owing to their multi-color emissions.[54]

The current work aims to exploit a novel fluorescent magnetic Gd_2O_3-based nanoprobe with an ultra-high relaxivity and multi-color cell imaging function, through a strategy of structure and dysprosium dopant modification. We synthesized the NPs *via* a facile chemical coprecipitation, and then characterized their morphology, structure and compositions subsequently. The influence of the shell thickness on the relaxation and the Dy^{3+} dopant concentration on the fluorescence properties has been systematically investigated. Furthermore, cytotoxicity assays, *in vitro* cell imaging and *in vivo* MRI detection of the tailored NPs are performed to find out whether it is safe for biomedical application as well as its efficacy as a dual-modal contrast agent. More details concerning the results can be viewed as the supporting information in the ESI† (Fig. S1–S11).

Experimental

Materials and reagents

All chemicals purchased were of analytical reagent grade and used as received without additional purification unless specified. Dysprosium nitrate hexahydrate ($Dy(NO_3)_3{\cdot}6H_2O$, 99.99%), gadolinium nitrate hexahydrate ($Gd(NO_3)_3{\cdot}6H_2O$, 99.9%) and ammonia solution (≥25%) were purchased from Sigma-Aldrich. Urea (≥99.0%) and ethanol (≥99.7%) were acquired from Guangzhou Chemical Reagent Factory. Tetraethyl orthosilicate (TEOS, ≥99.0%) was the product of China National Medicine Company. Magnevist (Gd-DTPA) was procured from Berlex Laboratories, Inc., USA. Ultra-pure Milli-Q water with an electrical resistivity of 18.25 MΩ cm (25 °C) was used throughout the experiments.

Fabrication of SiO_2 nanocores

We synthesized monodisperse silica nanospheres *via* a previously reported method[55] with some adjustments. After the hydrolysis of tetraethyl orthosilicate (TEOS, 3 ml) in an ethanol medium (100 ml) in the presence of water (2 ml) and ammonia (6 ml), the mixtures were stirred moderately at 40 °C for 24 h. The lacteal silica nanospheres were obtained and then re-dispersed in ethanol, and equally divided into six parts in six tubes after centrifugation and washing.

Encapsulation of SiO_2 with Gd_2O_3:Dy^{3+} nanoshells

The core–shell structured SiO_2@Gd_2O_3:Dy^{3+} NPs were fabricated by utilizing the following procedure. A tube of centrifuged SiO_2

NPs and 100 ml deionized water were placed into an Erlenmeyer flask and dispersed thoroughly. Then 3.0 g urea and 0.4 mmol of $Dy(NO_3)_3{\cdot}6H_2O$ and $Gd(NO_3)_3{\cdot}6H_2O$ with a varied relative molar ratio were dissolved into the lacteal mixtures and heated at 80 °C with vigorous agitation for 5 h. The precursors were obtained after centrifugation at 8000 rpm and washed with deionized water and ethanol, and then dried in a vacuum freeze drier. Finally, $SiO_2@Gd_2O_3{:}Dy^{3+}$ powders were successfully obtained after being heated at 800 °C in a furnace for 5 h.

Characterization

The core–shell structure, morphology, crystallinity and composition of the samples were measured using a thermal field emission scanning electron microscope (SEM, FEI Quanta 400F, 30 kV) equipped for energy dispersive X-ray spectroscopy (EDX), a transmission electron microscope (TEM, FEI Tecnai-G2 F30, 300 kV), an X-ray diffractometer (XRD, D-MAX 2200X VPC, 40 kV, 40 mA) and an X-ray photoelectron spectrometer (XPS, ESCALab250, 200 μm, 26 kV). The photoluminescence (PL) excitation and emission spectra were measured by using a spectrofluoro-photometer (FLS920, Edinburgh, 150 W xenon lamp) at room temperature.

Cytotoxicity assay

Cell viability was evaluated using cell counting kit-8 (CCK-8) assays. The cervical carcinoma HeLa cells and normal embryonic kidney 293 cells were selected to test the cytotoxicity of the $SiO_2@Gd_2O_3{:}Dy^{3+}$ NPs (1.0 mol%). A specific number of cells were seeded on 96-well plates and grown in the logarithmic phase at 37 °C with 5% CO_2 for 24 h in the culture media. The cells then were incubated with fresh culture media in the presence of various Gd^{3+} concentrations of the $SiO_2@Gd_2O_3{:}Dy^{3+}$ NPs and in the absence of the NPs as a negative control. After 48 h, 10 μl CCK-8 colorimetric solution was added into the wells and cultured for another 2 h at 37 °C with 5% CO_2. After removing the culture media, the absorbance of each well at 450 nm was measured on a microplate reader as a blank value, OD_{blank}. The culture media with CCK-8 were directly quantified by measuring the absorbance as a sample value, OD_{sample}. The absorbance was tested using a microplate photometer (MultiskanMK3, Waltham). The final optical density (OD) and the standard deviation values were measured in three independent repetitions. The relative cell viability (%) in the control wells was determined as the percentage ratio of the optical density in the culture medium containing nanoparticles at each concentration to that in the fresh control medium without any nanoparticles, which is calculated by the following formula:

$$\text{Cell viability} = \frac{OD_{sample} - OD_{blank}}{OD_{control}} \times 100\%, \quad (1)$$

where $OD_{control}$ is the absorbance of the negative control value.

Living cell confocal microscopy imaging

Human cervical HeLa cells were seeded in the wells of 24-well plates and grown in the logarithmic phase at 37 °C with 5% CO_2 in Dulbecco's modified Eagle's medium. Then the cells were incubated with the $SiO_2@Gd_2O_3{:}Dy^{3+}$ NPs in fresh culture media for another 1 h. After coincubation, the cells were washed with phosphate buffer solution (PBS) to remove the excess nanoparticles and dead cells, and then observed under a confocal laser microscope (Leica TCSSP8) operating at an excitation wavelength of 405 nm.

MR relaxation measurements

The longitudinal relaxivities (r_1) of the $SiO_2@Gd_2O_3{:}Dy^{3+}$ NPs were measured using a MRI system (MicroMR-18, Shanghai Niumag Corp., 0.55 T) in our Joint Laboratory of Sun Yat-sen University and Niumag Company. The samples with Gd^{3+} ion concentrations varying from 0 to 0.1 mM had a volume of 1.0 ml. The longitudinal relaxation times (T_1) in the presence of a commercial contrast agent Gd-DTPA or $SiO_2@Gd_2O_3{:}Dy^{3+}$ NPs at different concentrations were tested with inversion recovery (IR) pulse sequences. IR series for T_1: P90 (μs) = 11.00, P180 (μs) = 22.00, SW (kHz) = 50, TR (ms) = 2000, RG1 = 18, RG2 = 3, NS = 4, sampling number = 36. T_1 of each sample was determined from the exponential fitting curves plotted with the following non-linear least square regression equation:

$$S_{IR}(t) = S_0{*}[1 - 2\exp(-t/T_1) + \exp(-TR/T_1)], \quad (2)$$

by which the longitudinal relaxation times of the $SiO_2@Gd_2O_3{:}Dy^{3+}$ NPs with varied Gd^{3+} and Dy^{3+} concentrations were obtained. Here, TR is the time of repetition, a parameter in IR series. After that, the relaxivity (r_1) value was calculated according to the following equation:

$$R_1 = \Delta R_1/[Gd], \quad (3)$$

where R_1 is the relaxation rate ($R_1 = 1/T_1$, s^{-1}) and [Gd] is the concentration of the gadolinium ions (mM). Meanwhile, r_1 also can be worked out through the slopes of the curve linear fitting with the $1/T_1$ relaxation rate (s^{-1}) against Gd^{3+} concentration (mM).

In vitro and *in vivo* magnetic resonance imaging

In vitro and *in vivo* MRI data were acquired using a 0.5 T MRI system (MesoMR23-60H-I, Shanghai TestNiumag Corp.). All data were analyzed by picture archiving and communications system (PACS). A nude mouse (19.2 g) was provided by Shanghai Slack Experimental Center and animal experiments were carried out according to the National Institute of Health guidelines on the rules of animal research and the Institution's Animal Board. The mouse was anesthetized by intraperitoneal injection of 0.1% mebumalnatrium (10 μl per g weight) and kept at normal body temperature. Then $SiO_2@Gd_2O_3{:}Dy^{3+}$ NPs of 10.0 μmol kg in 100 μl of 0.4% PBS were injected into the mouse *via* the tail vein. T_1-weighted magnetic resonance imaging of the mouse before and after administering the NPs were performed with multi-layer spin echo (MSE) pulse sequences. The following parameters were adopted in the measurements. MSE series: SFO1 (MHz) = 23.315, P90 (us) = 3200, P180 (us) = 3200, TR (ms) = 400, TE (ms) = 9.5, slice width (mm) = 3, slice gap (mm) = 0.5, slices = 5, averages = 12.

Results and discussion

Synthesis and characterization of the core–shell nanoparticles

The synthesis protocol of the SiO_2@Gd_2O_3:Dy^{3+} nanopowders in the study is schematically illustrated in Fig. 2 and detailed in the Experimental section. The crystallinity and phase purity of the as-annealed samples were measured by X-ray powder diffraction (XRD) as shown in Fig. 3(a). The XRD pattern shows that all the peaks are well indexed to the cubic phase of Gd_2O_3 (PDF# 65-3181), and no impurity phases were observed within the detection limit of the XRD. The significant broadening of the peaks indicates the presence of NPs with a small crystalline size. The XRD patterns of the precursors can be viewed in Fig. S1 (ESI†). The X-ray photoelectron spectra (XPS) of the nanopowders are shown in Fig. 3(b and c), which were carried out to examine the oxidation states of Gd and Dy on the surface of the nanoshells. The emergence of a Dy $3d_{5/2}$ peak verifies that Dy^{3+} has been successfully doped into the host Gd_2O_3.

Fig. 4(a and c) display the typical transmission electron microscopy (TEM) and high resolution (HR) TEM images of the NPs. The particle has an excellent core–shell framework and a spherical shape with various degrees of surface roughness. The size distribution histogram shown in Fig. 4(b) reveals that the NPs have a mean diameter of 96.5 nm approximately. The selected area electron diffraction (SAED) of the NPs shown in Fig. 4(d) provides evidence of the polycrystalline structure with an excellent crystalline nature.

The results of scanning electron microscopy (SEM) and the energy dispersive X-ray spectra (EDX), as shown in Fig. S2 (ESI†), also demonstrate a superior sphericity and the existence of Dy^{3+} and Gd^{3+} in the NPs. Fourier transmission infrared (FTIR) spectra and thermo-gravimetry and differential thermal analysis (TG-DTA) shown in Fig. S3 and S4 (ESI†) can reflect the whole synthetic procedure and the product in every step, which can be related to the schematic illustration in Fig. 2.

Fluorescence and relaxation properties of the samples

Fig. 5(a) presents the photoluminescence excitation (inset one) and emission spectra of the SiO_2@Gd_2O_3:Dy^{3+} nanophosphors annealed at 800 °C. The excitation spectrum shows a broad band between 200 and 250 nm with two sharp absorption peaks. The former centered at approximately 230 nm results from the strong host ion absorption, mainly including electronic transitions from the O 2p valence band to the Gd 5d5s conduction band. The other broadband absorption at around 240 nm can be assigned to the oxygen-to-dysprosium charge transfer band (CTB), indicating that both the Gd_2O_3 host absorption band and the CTB contribute to the emissions of Dy^{3+} ions. The excitation peaks appeared at 255, 275, 310, 317 and 350 nm, and can be ascribed to typical f–f transition $^8S_{7/2}$–$^6D_{9/2}$, $^6I_{9/2}$, $^6P_{5/2}$, $^6P_{7/2}$ of Gd^{3+} and $^6H_{15/2}$–$^6P_{7/2}$ of Dy^{3+}. It is noted that the strongest excitation absorption appears at 275 nm, which transcends the host band absorption under 275 nm excitation; the emission spectrum consists of a group of lines at 485, 572, 612, 668 and 757 nm which are assigned to the characteristic energy transition from the excited state $^4F_{9/2}$ to the ground state ^6H_J (J = 15/2, 13/2, 11/2, 9/2, 7/2).

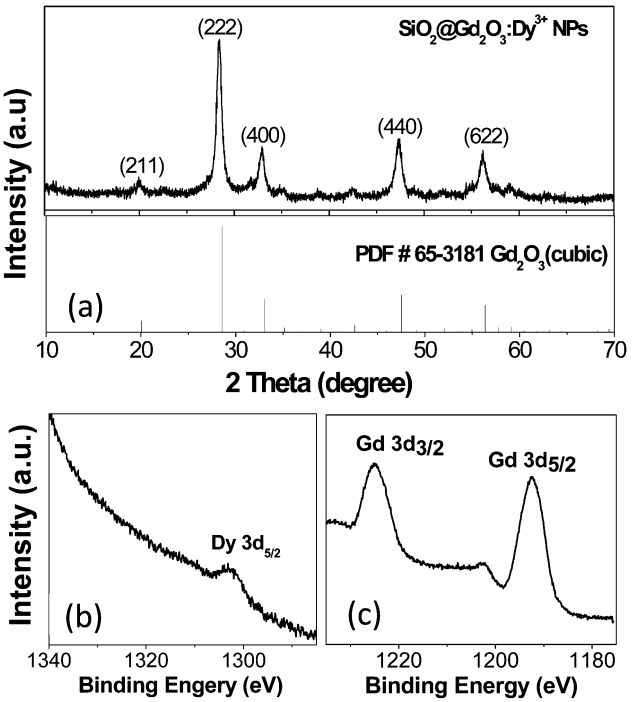

Fig. 3 (a) XRD of the sample and the standard cubic phase of Gd_2O_3, (b) Dy 3d XPS with a single peak at 1302 eV attributed to Dy in the trivalent state, (c) Gd 3d XPS with the binding energy of 1224 eV and 1191 eV assigned to Gd $3d_{3/2}$ and Gd $3d_{5/3}$ of Gd_2O_3, respectively (Dy/Gd ratio = 1.0 mol%).

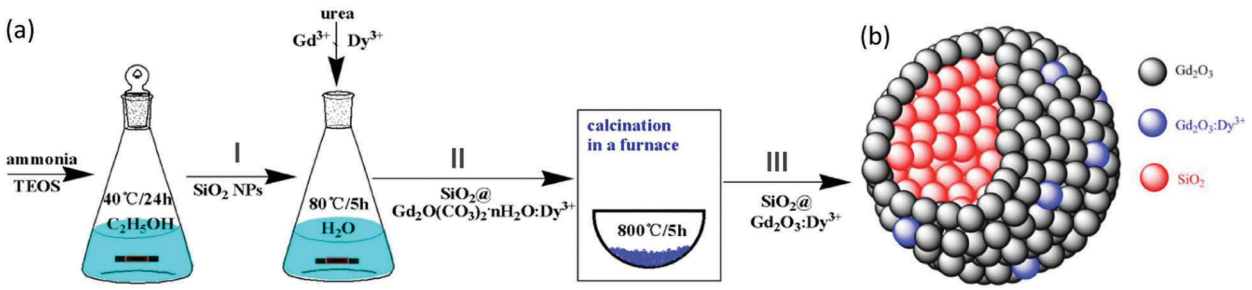

Fig. 2 (a) Scheme of the fabrication procedures and (b) the core–shell structure pattern of the as-synthesized SiO_2@Gd_2O_3:Dy^{3+} NPs. Three fabrication steps: (I) preparing SiO_2 NPs as the nanocores by the Stober method;[55] (II) depositing $Gd_2O(CO_3)_2$·nH_2O:Dy^{3+} NPs on the silica cores *via* a urea-based homogeneous precipitation; and (III) obtaining SiO_2@Gd_2O_3:Dy^{3+} NPs by annealing at 800 °C for 5 h.

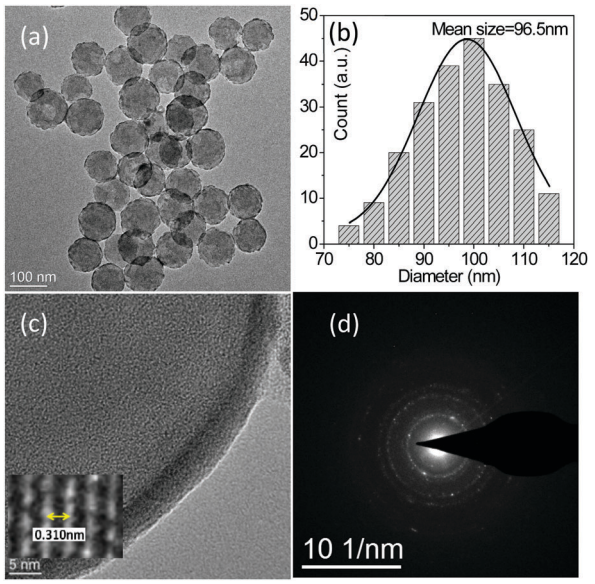

Fig. 4 (a) TEM image of the SiO_2@Gd_2O_3:Dy^{3+} NPs (Dy/Gd ratio = 1.0 mol%), (b) size distribution histogram with a mean diameter of approximately 96.5 nm obtained from Gaussian fitting (250 recognizable particles randomly chosen from some TEM images), (c) HR-TEM images of the NPs with the inset showing the clear lattice fringes with d = 0.310 nm exactly indexed as cubic Gd_2O_3 with (222) in the database (PDF# 65-3181), and (d) the corresponding SAED pattern of the NPs.

The possible corresponding energy transfer process occurring in the SiO_2@Gd_2O_3:Dy^{3+} samples, as we proposed, is schematically represented in Fig. 5(b). Under an excitation wavelength, photons in Gd_2O_3 are transferred from the ground state to the excited state. After a nonradiative energy decay from the excited states ^6D_J or ^6I_J to ^6P_J (J = 9/2, 7/2, 5/2...), the energy transfer occurs from the state of Gd^{3+} to the excited state $^6P_{7/2}$ of activator Dy^{3+}. The relative higher energy states are unstable, inducing a depopulation and subsequent nonradiative decay to the lower energy state $^4F_{9/2}$. Visible emissions then occur from the excited state $^4F_{9/2}$ back to the relevant ground states ^6H_J (J = 15/2, 13/2, 11/2, 9/2, 7/2). Besides, electrons located at the Gd 5d5s conduction band relax to the higher excited state $^6P_{7/2}$ after absorbing the energy of UV photons, and then transfer the energy to the activator Dy^{3+} ion.

The previous experimental reports[41–45,54] have demonstrated that cubic Gd_2O_3 is an excellent host lattice of the luminescence for activating other optical rare-earth ions. Owing to the relatively low phonon energy of Gd_2O_3, the rate of nonradiative transition will decrease, thus an increase in the luminescence efficiency of the host material has occurred. The Gd_2O_3 material calcined at 800 °C is a crystallographic sesquioxide with cubic bixbyite structures ($Ia\bar{3}$) which has two non-equivalent cationic sites with 6-fold coordination, as shown in Fig. 6. In the left structure called the C_2 site with non-inversion symmetry, the Gd^{3+} ion is placed in the center of a distorted cube with two oxygen vacancies lying on the face diagonals. Whereas in the right structure namely the S_6 site with inversion symmetry, two oxygen vacancies are located on one body diagonally. Numerous investigations[56] on the phosphor have reported that the ratio of

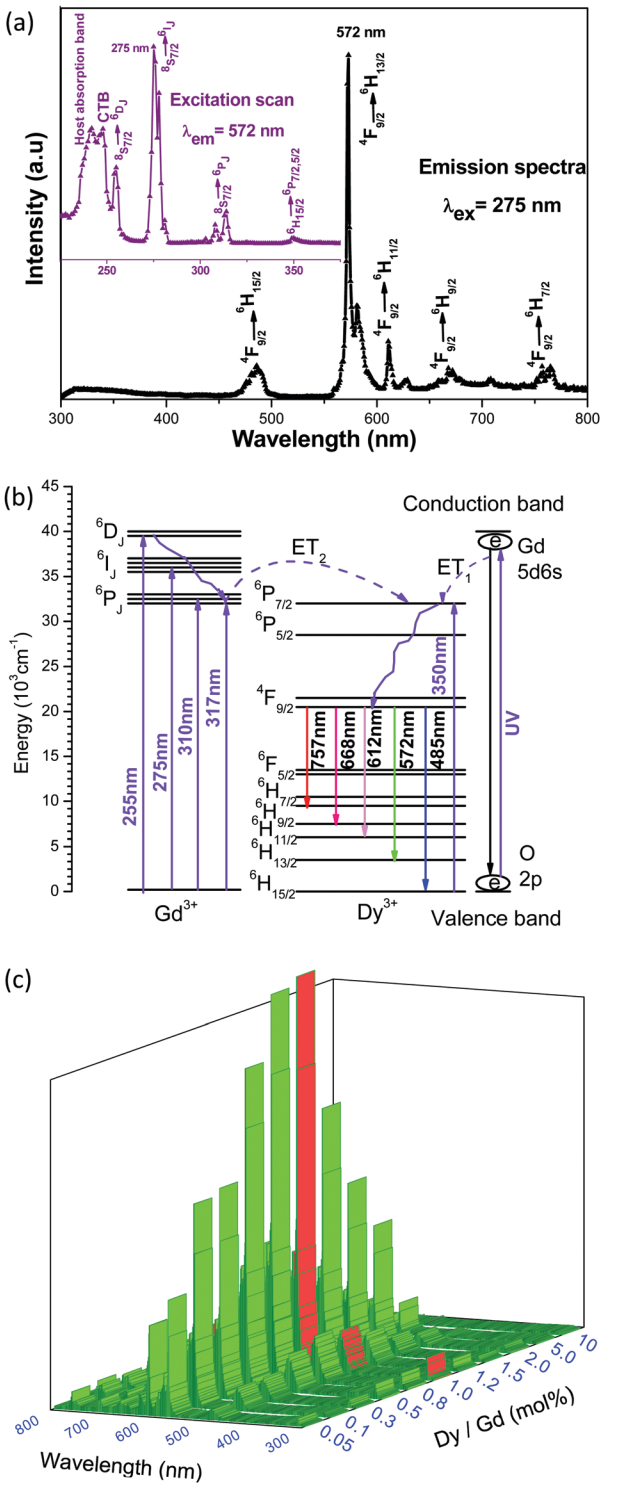

Fig. 5 (a) Excitation spectrum (left-top inset) obtained by monitoring the characteristic emission of the Dy^{3+} ions at 572 nm and recorded between 200 and 400 nm. Emission spectrum under 275 nm excitation of the SiO_2@Gd_2O_3:Dy^{3+} NPs (Dy/Gd ratio = 1.0 mol%), (b) the proposed energy transfer process, and (c) emission spectra of the SiO_2@Gd_2O_3:Dy^{3+} NPs with varied Dy dopant concentrations under the excitation wavelength of 275 nm.

Gd^{3+} ions occupying the C_2 to S_6 sites is 3 : 1 in general. The lanthanide ion Dy^{3+},[57] as an activator, has been widely exploited

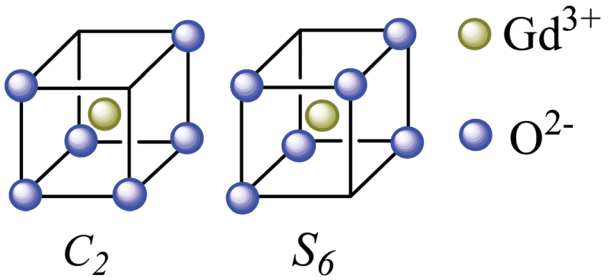

Fig. 6 Crystallographic sites in the Gd_2O_3 crystal structure. Left: C2 site with non-inversion symmetry; right: S_6 site with inversion symmetry.

in various host materials due to its unique multi-color luminescence properties. In Fig. 5(a), Dy^{3+} shows two dominant emission bands. The strongest yellow-green emission at 572 nm of the $^4F_{9/2}$ to $^6H_{13/2}$ transition is a parity forbidden electric dipole transition, which is hypersensitive and obviously varied with the local environment in the crystal. The other dominant blue emission occurring at 475 nm of the $^4F_{9/2}$ to $^6H_{15/2}$ transition belongs to magnetic dipole transitions and shows characteristic insensitivity to the surrounding environment. Because of the hypersensitive characteristics of the electric dipole transition at 572 nm ($^4F_{9/2}$ to $^6H_{13/2}$), if the Dy^{3+} ion is located at the non-symmetrical position (C_2 site), the yellow-green emission at 572 nm will be relatively strong. Furthermore, Fig. 5(c) presents the PL emission of SiO_2@Gd_2O_3 nanocrystals doped with Dy^{3+} ions at different contents. It can be noted that the representative emission peaks of Dy^{3+} remain unchanged in varied Dy^{3+} amounts. The shape and position of each band are similar but the intensities differ apparently. Herein, by increasing the Dy/Gd ratio, the emission intensity of Dy^{3+} monotonically enhances until the Dy^{3+} concentration is above 1.0 mol% and then it decreases gradually due to the concentration quenching of Dy^{3+} activators in the Gd^{3+} host lattice. It is because many more neighboring Dy^{3+} ions in the host structure would lead to cross-relaxation through resonance energy transfer.[58] As a result, the optimum concentration of Dy^{3+} was around 1.0 mol% in this case.

Due to the paramagnetic Gd^{3+} ions on the surfaces of the SiO_2@Gd_2O_3:Dy^{3+} NPs, they should serve as a positive signal enhancement MRI CA. The longitudinal relaxivity values of the NPs with different shell thicknesses have been evaluated (Fig. 7). According to the Solomon–Bloembergen–Morgan (SBM) theory,[28–33] the relaxation rate of water proton spinning in the presence of CAs is distance-dependent with $1/d^6$, where d is the relative distance between the water protons and Gd^{3+} ions. The SBM theory suggests that the shorter the distance is, the higher the relaxivity is. Compared to Gd^{3+} chelated by an organic molecule, the as-synthesized NPs with Gd^{3+} ions exposed on the surface are ligand-free, having a shorter distance and readily contacting with a larger number of water molecules, thereby facilitating more relaxed water in the vicinity rapidly exchanging with the other solvent water. In addition, this unique structure endows the nanocomposites with an extremely high surface to volume (S/V) ratio, namely a higher concentration of

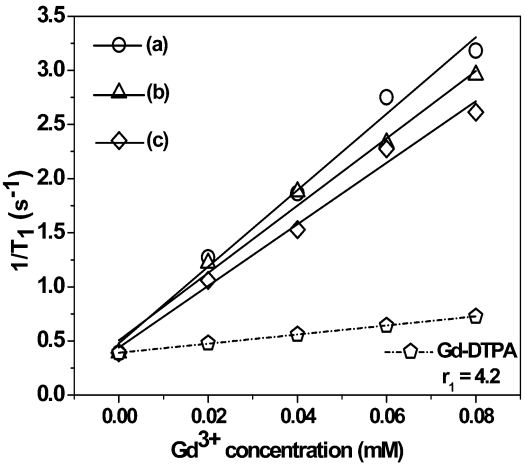

Fig. 7 The longitudinal relaxation rate *vs.* various molar concentrations of Gd-DTPA compared to the SiO_2@Gd_2O_3:Dy^{3+} NPs with different shell thicknesses. (a) 2 nm shell with r_1 of 34.47 mM^{-1} S^{-1}, (b) 5 nm shell with r_1 of 30.16 mM^{-1} S^{-1}, and (c) 10 nm shell with r_1 of 25.51 mM^{-1} S^{-1}.

Gd^{3+} ions on the surface of the Gd_2O_3 nanoshells, leading to a higher relaxation rate available. It means that a more efficient T_1 contrast enhancement is correlated with a thinner nanoshell of Gd_2O_3, which is justified with both schematic and mathematical illustrations in the ESI† (Fig. S5).

However, if the amount of Gd_2O_3 utilized for encapsulating silica is too low, parts of the SiO_2 nanospheres remain naked in the synthetic procedure, resulting in a waste of the cores, as shown in Fig. S6 (ESI†), and the corresponding TEM images of the NPs with a high volume of the raw reagent can be viewed in Fig. S7 (ESI†). Therefore, the obtained SiO_2@Gd_2O_3:Dy^{3+} NPs at a suitable shell thickness of 5 nm can satisfy the requirements of both complete core–shell architecture and rather high relaxivity of 30.16 mM^{-1} S^{-1}, which is almost 7 times larger than that of the clinical CAs, Gd-DTPA.

Toxicity and biocompatibility assays

In vitro cytotoxicity of the NPs was appraised with the cell counting kit solution (CCK-8) colorimetric assays using the normal embryonic kidney 293 cell line and the cervical carcinoma HeLa cell line. In the CCK-8 assays, the cell viability shown in Fig. 8 was measured using 2-(2-methoxyl-4-nitrophenyl)-3-(4-nitrophenyl)-5-(2,4-disulfo-phenyl)-2*H*-tetrazolium (WST-8), which is a water-soluble tetrazolium salt. The viability of negative control cells in the absence of the NPs is assumed as 100%. The normalized relative viability of the HeLa cell line in the presence of 10, 100, and 200 μg ml^{-1} NPs was estimated to be 103.4%, 107.6%, and 109.2% at 48 h, and that of the 293 cell line was calculated to be 102.1%, 92.7%, and 91.0%, respectively. Both HeLa and 293 cells in all cases exhibit regular viability compared to the negative control, even up to a high concentration of 200 μg ml^{-1}. The viability suggests that less than 10% HeLa cells were activated and more than 90% normal 293 cells remained living. All these results disclosed a negligible cytotoxicity, demonstrating a superior cytocompatibility of the hybrid NPs.

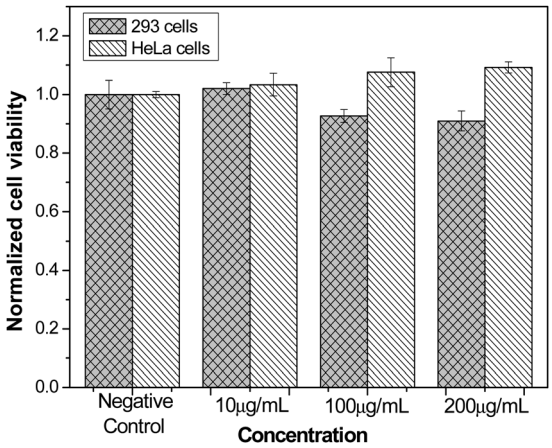

Fig. 8 Normalized cell viability of the normal embryonic kidney 293 cells and cervical carcinoma HeLa cells after incubation with various concentrations of SiO_2@Gd_2O_3:Dy^{3+} NPs after 48 h at 37 °C.

Overall, the *in vivo* toxicity of gadolinia-based NPs originates from either the dissociated toxic gadolinium ions or the severe aggregation of the NPs inside blood vessels, which is induced by both particular physical/chemical properties and the substantial specific surface area of nano-sized particles. The as-synthesized NPs possess good solubility at the commonly-used concentration according to the experimental observations, and the TEM images in Fig. 4 display their superior sphericity and dispersibility.

Therefore, the major threat to the living body of organisms is the leaking of gadolinium ions from the as-synthesized NPs. For patients with impaired renal function, an overdose of retained gadolinium ions in tissues may cause a rare potentially devastating syndrome of nephrogenic systemic fibrosis (NSF). In clinical bioapplication, the NPs can be coated with some biocompatible ligands for further reducing the risk of developing NSF, although the relaxivity of the NPs would decrease correspondingly. In this study, the ligand-free NPs also possess negligible Gd^{3+} leakage and can be used for *in vivo* application. In order to justify this, a specific *in vitro* Gd^{3+} leakage experiment was conducted in triplicate. The NPs were dispersed in physiological saline (sodium chloride (NaCl, 9 wt%) solution) for imitating an environment analogous to a living body. The concentration of gadolinium ions was determined as 50, 500, 5×10^3, 5×10^4 mg l^{-1}, respectively. The colloidal suspensions were ultrasonically dispersed for 30 min and continuously stirred at 37 °C for 48 h. The final suspensions were then centrifuged in the separated state, and the aqueous solutions were tested utilizing inductively coupled plasma mass spectroscopy (ICP-MS) to determine the concentration of free Gd^{3+} and Dy^{3+} ions. The results are displayed in Table 1 and negligible Gd^{3+} and Dy^{3+} ions have been detected simultaneously. For exploring the stability of the particles, we devised another

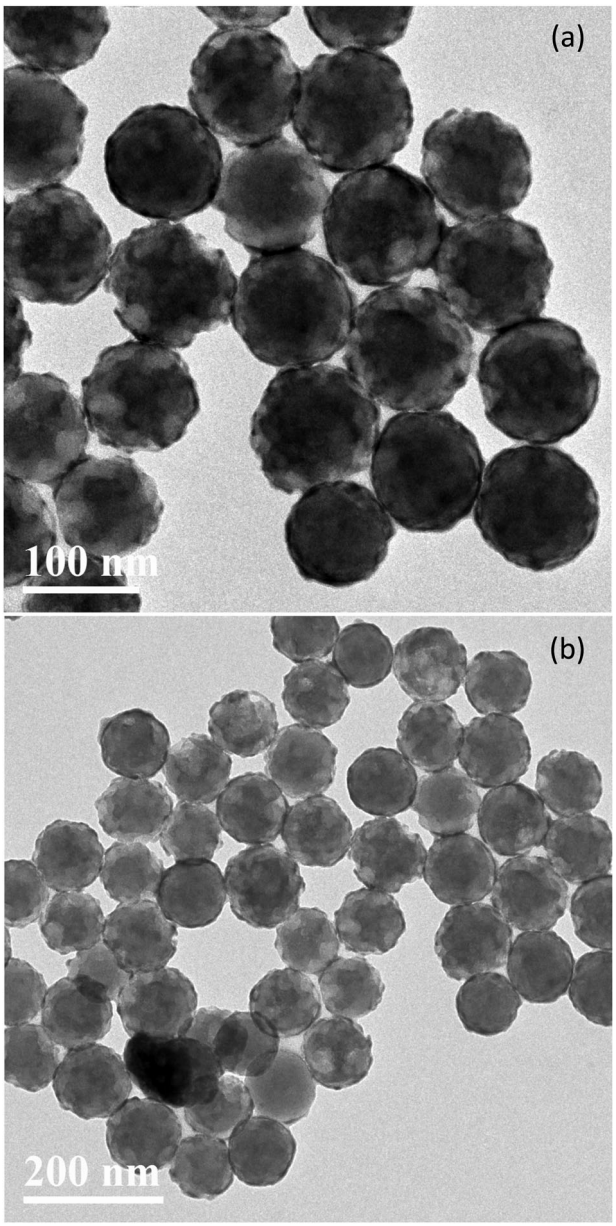

Fig. 9 TEM images of SiO_2@Gd_2O_3:Dy^{3+} NPs (Dy/Gd ratio = 1.0 mol%) before (a) and after (b) dispersing in physiological saline for four weeks.

Table 1 Gd^{3+} and Dy^{3+} leaking of the SiO_2@Gd_2O_3:Dy^{3+} NPs (Dy/Gd ratio = 1.0 mol%) in a physiological saline solution

Gd concentration in suspension (mg l^{-1})	Concentration of leaking Gd^{3+} (mg l^{-1})	Relative Gd^{3+} leakage	Dy concentration in suspension (mg l^{-1})	Concentration of leaking Dy^{3+} (mg l^{-1})	Relative Dy^{3+} leakage
50	—	—	5×10^{-1}	—	—
5×10^2	0.021	4.2×10^{-5}	5	—	—
5×10^3	0.244	4.9×10^{-5}	50	—	—
5×10^4	0.802	1.6×10^{-5}	5×10^2	0.014	2.8×10^{-5}

specific *in vitro* experiment. The NPs were stirred with physiological saline at 40 °C for 48 h and mixed for four weeks. Then TEM observation of the NPs before and after this duration was carried out. The results are displayed in Fig. 9 as TEM images. There are almost no changes observable in them, revealing good stability in physiological saline. Meanwhile, we conducted another facile experiment to explore the solubility of the SiO_2@Gd_2O_3:Dy^{3+} NPs. The NPs were ultrasonically dispersed in physiological saline aqueous solution to form colloidal suspensions with various concentrations. The colloidal suspensions were displaced into several transparent beakers. Keeping the beakers still for 2, 6 and 12 h, we observed and recorded the state of the suspensions using a camera. The results are shown in Fig. S8 (ESI†), demonstrating a certain water-solubility of the SiO_2@Gd_2O_3:Dy^{3+} NPs. Almost no precipitates were produced in the suspensions of the NPs even at a high Gd^{3+} dosage of 200 mg l^{-1}. The colloidal suspensions of the NPs with the commonly-used concentration of 20 mg l^{-1} (μg ml^{-1}) for *in vitro* and *in vivo* bioapplications are close to the pure physiological saline aqueous solution for a long time. The NPs readily dissolved in aqueous solutions due to the strong affinity between the oxide nanoscale particles and water. All these results reveal that the as-synthesized core–shell NPs possess superior biocompatibility and a high potential to be used as *in vivo* nanoagents.

Living cell fluorescence imaging

For assessing the feasibility of using the SiO_2@Gd_2O_3:Dy^{3+} nanoparticle agents with an optimized Dy^{3+} dose of 1 mol% as a potential fluorescence imaging probe for cellular studies, an *in vitro* bioassay was conducted by using the cervical carcinoma HeLa cell line incubated with 20 μg ml^{-1} agents for 2 h. The cells were imaged utilizing a confocal laser scanning microscope with an excitation wavelength of 405 nm and emission wavelength in three different ranges, which can be considered as a qualitative and highly efficient assessment of the samples taken up by the living cells. Fig. 10 shows clear blue and green fluorescence images with the emission wavelength in the range of 450 to 500 nm and 500 to 570 nm, as well as a slightly weak red fluorescence image with the emission wavelength above 600 nm. In addition to the commonly used RGB fluorescence imaging, we tuned the emission wavelength in the region of 570 to 590 nm and obtained a yellow fluorescence image (Fig. S9, ESI†). The results suggest that the NPs possess the functionality of multi-color living cell imaging and display different fluorescence images in various cases. Although the previous excitation spectrum reveals the optimal excitation wavelength of 275 nm in the UV region, all bright blue and green intracellular fluorescence can be still observed clearly

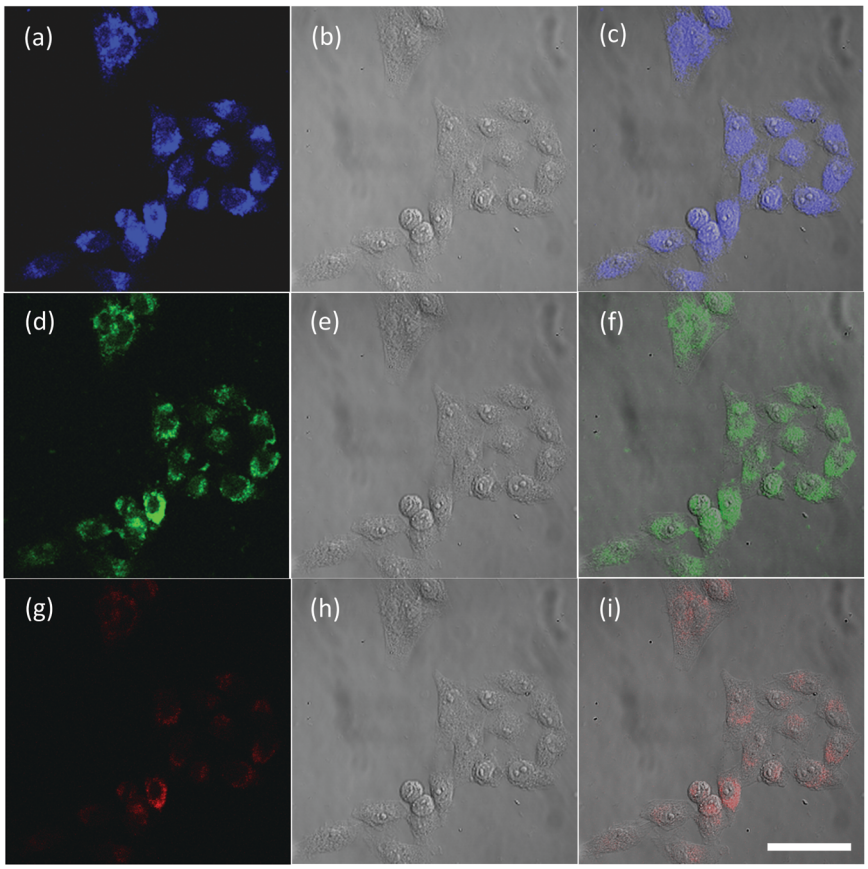

Fig. 10 Confocal microscopy images of HeLa cells incubated with 20 μg ml^{-1} SiO_2@Gd_2O_3:Dy^{3+} NPs (Dy/Gd ratio = 1.0 mol%) for 2 h. (a, d and g) Fluorescence images under irradiation of 405 nm light with blue, green and red emission channels. (b, e and h) Bright-field images. (c, f and i) Superimposed images. (Scale bar: 50 μm; image size: 212.13 μm × 212.13 μm.)

under irradiation of 405 nm light. The photo-luminescence excitation and emission spectra (Fig. S10, ESI†) under 405 nm excitation exhibit strong blue and green as well as weak yellow and red emissions, which are in good agreement with those in living cell fluorescence images. The bright-field (Fig. 10(b, e and h)) and the corresponding fluorescence images superimposed on the bright field (Fig. 10(c, f and i)) demonstrate that the cells are viable without any observable damage and the NPs have been taken up by the cells and still maintain the intrinsic fluorescence properties significantly. Furthermore, the visible blue, green, yellow and red emissions from the superimposed images are mainly distributed in the cytoplasm and the membrane surface of the living cells. The successful cellular internalization and the bright visible intracellular fluorescence indicate that the as-synthesized NPs will be potential candidates as a fluorescence nanoprobe for *in vivo* bioimaging and biolabelling.

T_1-weighted MRI study of mice

In vitro and *in vivo* T_1-weighted MRI and the pseudo color images of the as-designed NPs are shown in Fig. 11 and Fig. S11 (ESI†). An *in vitro* MRI image of Gd-DTPA was obtained for comparison with that of the NPs, as shown in Fig. 11(a). Significant contrast enhancements during imaging were observed in the liver and kidneys of the mouse. The images were obtained using a 0.5 T clinical MRI system by intravenous injection of SiO_2@Gd_2O_3:Dy^{3+} NPs with a dose of 10 μmol kg^{-1} into the tail vein of the mouse.

At 30 min, the enhancement signals in the kidneys and the liver are much more intense than those of the control image at the start, signifying the feasibility of applying the as-synthesized NPs as both hepatic and renal CAs *via* passively targeted accumulation in the liver and kidneys. After 120 min, the imaging signals decline in comparison to the former, especially in the kidneys. The signal decrease in the liver is slighter due to the rather long clearance time of the hybrid NPs through the reticuloendothelial system of the liver. According to our previous pharmacokinetics and pharmacodynamics of 100 nm gadolinium-based nanocomposites, the NPs are excreted *via* the hepatobiliary pathway within several weeks. And the blood circulation half-life is about 90 min. Due to their large size, the NPs cannot be cleared by glomerular filtration in the kidneys. Despite the long excretion life, almost all the NPs would be cleared after several weeks, followed by a gradual decrease in further excretion. After the experiment, the mice survived normally. These *in vivo* results suggest that the NPs are potential candidates as clinical T_1-weighted MRI contrast agents.

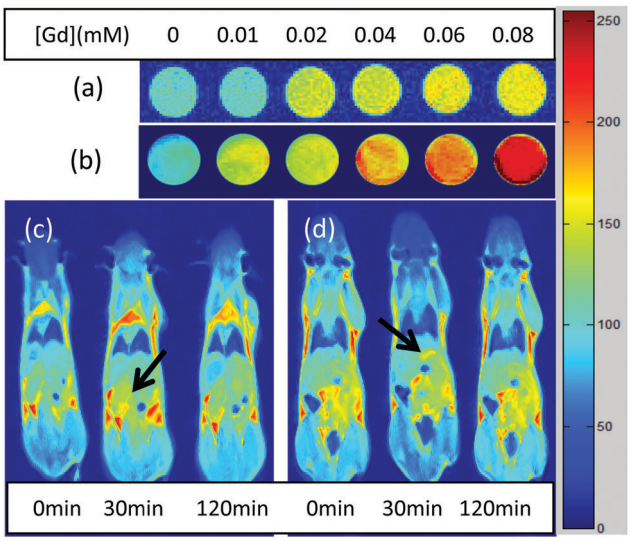

Fig. 11 *In vitro* and *in vivo* T_1-weighted MR images of SiO_2@Gd_2O_3:Dy^{3+} NPs (Dy/Gd ratio = 1.0 mol%). (a) MR phantom images of Gd-DTPA with varied Gd concentrations. (b) MR phantom images of the NPs with varied Gd concentrations. (c) Signal intensity changes in the kidney and (d) liver of a nude mouse before and after injection of the sample (10 μmol kg^{-1}, smaller than that of the standard Gd-DTPA of 0.1–0.2 mmol kg^{-1}) measured at varied times.

Conclusions

We have successfully synthesized core–shell structured SiO_2@Gd_2O_3:Dy^{3+} nanoparticles with an average diameter of approximately 96.5 nm and a uniform size distribution and superior dispersibility *via* a urea-based chemical coprecipitation method. After being doped with 1.0 mol% Dy^{3+} ions, the as-obtained nanophosphors exhibit the most intense yellow-green emission under 275 nm excitation. The multi-color emission spectrum consists of a group of lines at 485, 572, 612, 668 and 757 nm, respectively, which are assigned to the characteristic energy transition from the excited state $^4F_{9/2}$ to the ground state ^6H_J (J = 15/2, 13/2, 11/2, 9/2, 7/2) according to the proposed possible energy transfer process. A strategy to design the core–shell structure with an ultra-thin nanoshell has been proposed in light of the Solomon–Bloembergen–Morgan theory and thereby an ultra-high longitudinal relaxivity of 30.16 mM^{-1} S^{-1} has been achieved in the case of keeping an integrated core–shell architecture. The measured relaxation rates of the samples were almost 7 times higher than the counterpart of the commercial contrast agent Gd-DTPA in a 0.55 T MR system. *In vitro* cytotoxicity tests based on the CCK-8 assay reveal that the as-synthesized SiO_2@Gd_2O_3:Dy^{3+} nanoagent has a low toxicity and satisfactory biocompatibility. The clear *in vitro* living cell multi-color images and distinctive *in vivo* MR images in a mouse demonstrate that the as-designed nanoparticles have excellent potential to be developed into a safe and effective dual-modal contrast material for magnetic resonance and fluorescence combined imaging.

Acknowledgements

This study was supported by the National Natural Science Foundation of China (grant no. 11273494), the Fundamental Research Funds for the Central Universities (grant no. 11lgjc12) and the Specialized Research Fund for the Doctoral Program of Higher Education (grant no. 20110171110023). The authors would like to acknowledge Shanghai R&S Biotechnology Co., Ltd and Suzhou Niumag Analytical Instrument Corporation for their help in bioassays. In particular, the author Jinchang Yin is

thankful to Dr Dekang Xu and Anming Li for their discussion on photoluminescence.

Notes and references

1 K. Emblem, C. Farrar, E. Gerstner, T. Batchelor, R. H. Borra, B. Rosen, A. Sorensen and R. Jain, *Nat. Rev. Clin. Oncol.*, 2014, **11**, 566–584.
2 S. Kunjachan, J. Ehling, G. Storm, F. Kiessling and T. Lammers, *Chem. Rev.*, 2015, **115**, 10907–10937.
3 P. Hemmer, *Science*, 2013, **339**, 529–530.
4 A. A. Lysova and I. V. Koptyug, *Chem. Soc. Rev.*, 2010, **39**, 4585–4601.
5 W. B. Hyslop and R. C. Semelka, *Top. Magn. Reson. Imaging*, 2005, **16**, 3–14.
6 E. L. Que and C. J. Chang, *Chem. Soc. Rev.*, 2010, **39**, 51–60.
7 W. B. Hyslop, N. C. Balci and R. C. Semelka, *Magn. Reson. Imaging Clin. N. Am.*, 2005, **13**, 211–224.
8 S. Aime, M. Fasano and E. Terreno, *Chem. Soc. Rev.*, 1998, **27**, 19–29.
9 H. Abdel-Aty, O. Simonetti and M. G. Friedrich, *J. Magn. Reson. Imaging*, 2007, **26**, 452–459.
10 J. Gallo, N. J. Long and E. O. Aboagye, *Chem. Soc. Rev.*, 2013, **42**, 7816–7833.
11 Y. Dai, A.-P. Zhang, J. You, J.-J. Li, H.-T. Xu and K. Xu, *RSC Adv.*, 2015, **5**, 77204–77210.
12 M. Bottrill, L. Kwok and N. J. Long, *Chem. Soc. Rev.*, 2006, **35**, 557–571.
13 M.-A. Fortin, R. M. Petoral Jr, F. Söderlind, A. Klasson, M. Engström, T. Veres, P.-O. Käll and K. Uvdal, *Nanotechnology*, 2007, **18**, 395501.
14 T. S. Atabaev, J. H. Lee, D.-W. Han, H.-K. Kim and Y.-H. Hwang, *RSC Adv.*, 2014, **4**, 34343–34349.
15 N.-Q. Luo, X.-M. Tian, J. Xiao, W.-Y. Hu, C. Yang, L. Li and D.-H. Chen, *J. Appl. Phys.*, 2013, **113**, 164306.
16 A. Radbruch, L. D. Weberling, P. J. Kieslich, O. Eidel, S. Burth, P. Kickingereder, W. Wick, H.-P. Schlemmer and M. Bendszus, *Radiology*, 2016, **279**, 323–326.
17 K. B. Beckett, A. K. Moriarity and J. M. Langer, *RadioGraphics*, 2015, **35**, 1738–1750.
18 T. Kanda, T. Fukusato, M. Matsuda, K. Toyoda, H. Oba, J. Kotoku, T. Haruyama, K. Kitajima and S. Furui, *Radiology*, 2015, **276**, 228–232.
19 N. Karabulut, *RadioGraphics*, 2016, **36**, 620–621.
20 M. Kircher, A. Zerda, J. Jokerst, C. Zavaleta, P. Kempen, E. Mittra, K. Pitter, R. Huang, C. Campos, F. Habte, R. Sinclair, C. Brenman, I. Mellinghoff, E. Holland and S. Gambhir, *Nat. Med.*, 2012, **18**, 829–834.
21 N. Bloembergen, E. M. Purcell and R. V. Pound, *Phys. Rev.*, 1948, **73**, 679–712.
22 I. Solomon, *Phys. Rev.*, 1955, **99**, 559–565.
23 L. O. Morgan and A. W. Nolle, *J. Chem. Phys.*, 1959, **31**, 365–368.
24 N. Bloembergen, *J. Chem. Phys.*, 1957, **27**, 572–573.
25 R. B. Lauffer, *Chem. Rev.*, 1987, **87**, 901–927.
26 P. F. Cox and L. O. Morgan, *J. Am. Chem. Soc.*, 1959, **81**, 6409–6412.
27 P. Caravan, *Chem. Soc. Rev.*, 2006, **35**, 512–523.
28 P. Caravan, J. J. Ellison, T. J. McMurry and R. B. Lauffer, *Chem. Rev.*, 1999, **99**, 2293–2352.
29 A. Gizzatov, M. H. Rivera, V. Keshishian, Y. Mackeyev, J. J. Law, A. Guven, R. Sethi, F. Qu, R. Muthupilai, M. Hansen, J. T. Willerson, E. C. Perin, Q. Ma, R. G. Bryant and L. J. Wilson, *Nanoscale*, 2015, **7**, 12085–12091.
30 N.-Q. Luo, X.-M. Tian, C. Yang, J. Xiao, W.-Y. Hu, D.-H. Chen and L. Li, *Phys. Chem. Chem. Phys.*, 2013, **15**, 12235–12240.
31 D. Sage, K. Arai, D. R. Glenn, S. J. DeVience, L. M. Pham, L. R. RahnLee, M. D. Lukin, A. Yacoby, A. Komeili and R. L. Walsworth, *Nature*, 2013, **496**, 486–489.
32 A. Louie, *Chem. Rev.*, 2010, **110**, 3146–3195.
33 G. Choy, P. Choyke and S. K. Libutti, *Mol. Imaging*, 2003, **2**, 303–312.
34 X.-Y. Kuang, H. Liu, W.-Y. Hu and Y.-Z. Shao, *Dalton Trans.*, 2014, **43**, 12321–12328.
35 S. A. Corr, A. Byrne, Y. K. Gun'ko, S. Ghosh, D. F. Brougham, S. Mitchell, Y. Volkov and A. P. Mello, *Chem. Commun.*, 2006, 4474–4476.
36 M. Cho, E. Q. Contreras, R. Sethi, S. S. Lee, C. J. Jones, W. Jang and V. L. Colvin, *J. Phys. Chem. C*, 2014, **118**, 14606–14616.
37 A. M. Gobin, E. M. Watkins, E. Quevedo, V. L. Colvin and J. L. West, *Small*, 2010, **6**, 745–752.
38 M. Baker, *Nature*, 2010, **463**, 977–980.
39 N.-Q. Luo, C. Yang, X.-M. Tian, J. Xiao, J. Liu, F. Chen, D.-H. Zhang, D.-K. Xu, Y.-L. Zhang, G.-W. Yang, D.-H. Chen and L. Li, *J. Mater. Chem. B*, 2014, **2**, 5891–5897.
40 E. Terreno, D. D. Castelli, A. Viale and S. Aime, *Chem. Rev.*, 2010, **110**, 3019–3042.
41 X. Lim, *Nature News*, 2016, **531**, 26–28.
42 J. Zhou, Q. Liu and F. Li, *Chem. Rev.*, 2015, **116**, 395–464.
43 A.-M. Li, D.-K. Xu, H. Lin, S.-H. Yang, Y.-Z. Shao, Y.-L. Zhang and Z.-Q. Chen, *RSC Adv.*, 2015, **5**, 45693–45702.
44 J.-C. Yin, C.-R. Li, Y.-B. Yang, W.-Y. Hu, H. Liu and Y.-Z. Shao, *RSC Adv.*, 2016, **6**, 72836–72844.
45 J. Liu, H.-W. Deng, Z.-Y. Huang, Y.-L. Zhang, D.-H. Chen and Y.-Z. Shao, *Phys. Chem. Chem. Phys.*, 2015, **17**, 15412–15418.
46 W. Cai, A. R. Hsu, Z.-B. Li and X. Chen, *Nanoscale Res. Lett.*, 2007, **2**, 265–281.
47 X. Gao, Y. Cui, R. M. Levenson, L. W. K. Chung and S. Nie, *Nat. Biotechnol.*, 2004, **22**, 969–976.
48 W. Wang, F. Aldeek, X. Ji, B. Zeng and H. Mattoussi, *Faraday Discuss.*, 2014, **175**, 137–151.
49 I. L. Medintz and H. Mattoussi, *Phys. Chem. Chem. Phys.*, 2009, **11**, 17–45.
50 B. Kumar, I. Roy, T. Y. Ohulchanskyy, L. N. Goswamt, A. C. Binilu, E. J. Bergey, K. M. Tramposch, A. Maltra and P. N. Prasad, *ACS Nano*, 2008, **2**, 449–456.
51 S. Kim, T. Y. Ohulchanskyy, H. E. Pudavar, R. K. Pandey and P. N. Prasad, *J. Am. Chem. Soc.*, 2007, **129**, 2669–2675.
52 S. Kim, H. E. Pudavar, A. Bonoiu and P. N. Prasad, *Adv. Mater.*, 2007, **19**, 3791–3795.

53 W.-Y. Hu, H. Liu and Y.-Z. Shao, *New J. Chem.*, 2015, **39**, 7363–7371.
54 T. Selvalakshmi, S. Sellaiyan, A. Uedono and A. C. Bose, *RSC Adv.*, 2014, **4**, 34257–34266.
55 W. Stober, A. Fink and E. Bohn, *J. Colloid Interface Sci.*, 1968, **26**, 62–65.
56 G. Blasse and A. Bril, *Philips Res. Rep.*, 1966, **21**, 368.
57 Q. Su, H. Liang, C. Li, H. He, Y. Lu, J. Li and Y. Tao, *J. Lumin.*, 2007, **122–123**, 927–930.
58 J. Raju, E. Pavitra and J. Yu, *Dalton Trans.*, 2013, **42**, 11400–11410.

